DOI:
10.1002/jbio.202200028

Document Version
Peer reviewed version

Optical birefringence changes in myelinated and unmyelinated nerves: a comparative study

JOAQUIN CURY*,[1,2] HUGO SMETS,[2] CAROLINE BOUZIN,[3] PASCAL DOGUET,[4] ANNE VANHOESTENBERGUE,[5] JEAN DELBEKE,[6] RIËM EL TAHRY,[6] ANTOINE NONCLERCQ,[2] SIMON-PIERRE GORZA[1]

[1] *Opera-photonics, Université libre de Bruxelles, Belgium.*
[2] *Bio-, Electro- and Mechanical Systems (BEAMS), Université libre de Bruxelles, Belgium.*
[3] *Université Catholique de Louvain - Institut de Recherche Expérimentale et Clinique (IREC), IREC Imaging Platform (2IP), Belgium.*
[4] *Synergia Medical, Mont-Saint-Guibert, Belgium.*
[5] *Aspire Centre for Rehabilitation Engineering and Assistive Technology, University College of London, UK.*
[6] *Institute of Neurosciences (IONS), Université Catholique de Louvain - Cliniques Universitaires Saint Luc, Department of Neurology, Belgium.*

Abstract: The measurement of birefringence variations related to nerve activity is a promising label-free technique for sensing compound neural action potentials (CNAPs). While widely applied in crustaceans, little is known about its efficiency on mammal peripheral nerves. In this work, birefringence recordings to detect CNAPs, and Stokes parameters measurements were performed in rat and lobster nerves. While single-trial detection of nerve activity in crustaceans was achieved successfully, no optical signal was detected in rats, even after extensive signal filtering and averaging. The Stokes parameters showed that a high degree of polarization of light is maintained in lobster sample, whereas an almost complete light depolarization occurs in rat nerve. Our results indicate that depolarization itself is not sufficient to explain the absence of birefringence signals in rats. We hypothesize that this absence comes from the myelin sheets which constraint the birefringence changes to only take place at the nodes of Ranvier.

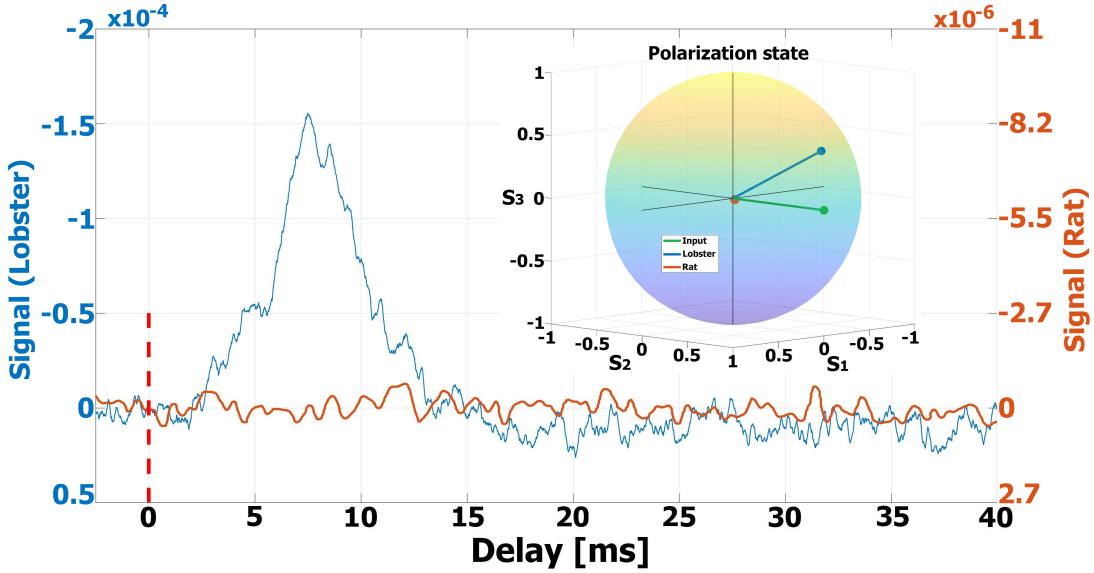

Keywords: Birefringence, nerve, electric stimulation, multiple scattering, Stokes vector, compound neural action potential monitoring.

Correspondence: joaquin.cury@ulb.be

1 INTRODUCTION

Neurostimulation is one of the fastest-growing areas of medicine that has been approved for the treatment of several debilitating conditions, including refractory epilepsy [1], chronic pain [2], Parkinson's disease [3], depression [4], gastroparesis [5] and tremors [6]. Moreover, this method is still under investigation for other pathologies, such as obesity [7], migraine [8] and heart failure [9].

The monitoring of nerve activity as a marker for these disorders has grown in importance. Electrical recording is still the traditional technique for acquiring compound neural action potentials (CNAPs). This approach has, however, several limitations. High-density microelectrodes arrays located on the surface of neural tissues have a spatial resolution limited by the number and spacing of electrodes [10]. Moreover, mechanical strains at the tissue-electrode interface might cause inflammation and neural degeneration [11]. This also leads to mechanical damages of the electrodes, resulting in a loss of the recording sensitivity [11]. Penetrating electrodes are not suitable for clinical applications due to their invasiveness [12]. In implanted electrostimulators, the metallic leads and electrodes have the major drawback of being incompatible with magnetic resonance imaging (MRI) because of their sensitivity to the magnetic field and the induction heat production [13].

A possible alternative solution to overcome these limitations is optical sensing. Several methods are currently available for optical monitoring of CNAPs. Some of these techniques use dyes [14–17]. However, these are not suitable for use in clinical applications. Alternatively, there are label-free methods such as light scattering [18], birefringence [19], infrared spectroscopy [20], laser interferometric microscopy [21] and optical coherence tomography (OCT) [22]. These are based on the detection of fast intrinsic optic signals (IOS) variations related with nerve activity. In this context, IOS are the result of optical properties alterations caused by cellular swelling and structure conformation changes such as the reorientation of membrane proteins and phospholipids [10,12,19,23].

Methods relying on birefringence changes related to nerve activity have attracted a lot of attention in crustacean nerves [19] in which they provide a larger optical signal for CNAP detection compared to scattering-based techniques, allowing single-trial measurements of CNAPs. They have been implemented extensively in invertebrate nerves, whereas there is a lack of studies in mammals. Ex-vivo birefringence measurements have been performed in lobster [10,12,19,23], squid [24], crayfish [19], crabs [24], mouse brain dendrites [25], and tentatively in mice sciatic nerves [26].

The use of this technique in mammal peripheral nerves is particularly important for translational research. However, these nerves exhibit unfavorable structural features in terms of myelination as well as number and diameter of axons [27,28], which increase light scattering (Figure 1). This could reduce the effectiveness of birefringence-based methods [23].

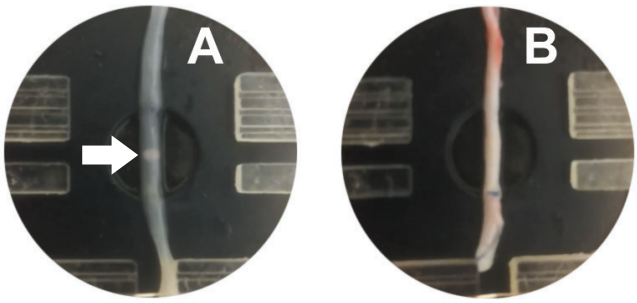

Fig. 1 A: Lobster walking leg nerve. B: Rat sciatic nerve, main trunk. Both samples have the same thickness ($\approx$ 0.9 mm). The 1 mm diameter pinhole over which the nerves are placed can be seen as a white dot in A (white arrow), thanks to the relative transparency of the crustacean sample. This is not the case in B, due to the opacity of the nerve.

In the present study, we performed ex-vivo birefringence recordings in transmission mode to detect CNAPs, both in lobster nerves and rat sciatic nerves. Stokes parameters were also measured at the same location to analyze the state of polarization of the output light in the nerve resting state. Employing the Stokes-Mueller formalism, we linked the cross-polarized signal to the retardance change during the CNAP and derived the signal-to-noise ratio. We determined to what extent, light depolarization could prevent optical monitoring of CNAPs, both in unmyelinated and myelinated nerves.

2 MATERIALS AND METHODS

All ex-vivo experiments were performed at the Opera photonics Laboratory, Université libre de Bruxelles (ULB), Belgium. The surgery in rats was conducted at the Institute of Neuroscience (IONS), Université Catholique de Louvain (UCL), Belgium, which has access to an animal care facility accredited by the Animal Care Service of the Federal Public Department. This work fully complies with a protocol (2019/UCL/MD/007) approved by the ethics committee for animal experimentation at UCL, in agreement with the ETS 123 European Convention.

2.1 Nerve dissection and preparation

Nerves from lobster Homarus Gammarus claws, first and second rostral legs were removed using the Furusawa pull-out technique [29]. To avoid any cytoplasm leakage and allow to gently handle the sample, the edges were tied using a piece of suture thread. After the removal, the nerve was immersed in Homarus Ringer's solution (523 mM NaCl, 5 mM Glucose, 13.3 mM KCl, 12.4 mM CaCl2 and 24.8 mM MgCl2, pH 7) at

4°C [12], during 10 – 15 minutes. Male Wistar rat sciatic nerves were dissected following the procedures described in [30]. We paid special attention to remove all the connective tissue surrounding the sample in order to avoid scattering from other tissues than the nerve. After the nerve had been tied on each extremity, it was left to recover at room temperature for about 20 minutes in Hepes-buffered oxygenated Krebs Ringer solution (140 mM NaCl, 5 mM KCl, 2 mM CaCl2, 1 mM MgCl2, 5.5 mM HEPES, 11 mM D-glucose, pH 7.3, Fisher Scientific, Belgium) gassed with pure oxygen (3 l/min during 120 minutes) before the start of recordings.

2.2 Experimental setup

The setup is made of five main blocks: (i) a nerve chamber coupled to an optical setup for measuring CNAPs, (ii) an incoherent light source, (iii) an electrical channel for electrical stimulation and recording; (iv) an optical channel with a photodiode in a transimpedance amplifier followed by two amplifier stages, each with a bandpass filter to limit the noise; and (v) a digital-to-analog converter to record the signal from the electrical and the optical channels.

2.2.1 Nerve chamber and electrodes position

The nerve chamber (NC) was designed in Solidworks 2020 (Solidworks Corp., USA) and built from a photopolymer resin using a 3D printer (Objet Eden260VS, Stratasys). Figure 2 shows the printed NC. The chamber can hold nerves of different thicknesses and lengths. In the middle of the NC is a circular section that slots over a stainless steel plate with a precisely cut pinhole of 0.5 or 1 mm diameter (P500D or P1000K, Thorlabs, Germany) to constrain the light beam to a well-defined diameter. For electrical stimulation and recording of CNAPs, five electrodes, hosted in grooves, were used (99.99% silver wire, diameter 250 μm, Sigma Aldrich, Belgium). Two of them for stimulation (anode and cathode) and the remaining three for recording (GND: ground, CNAP+ and CNAP-). The distance between electrodes of the same group ranged 1.4 to 3 mm. For lobster nerves, the distance between cathode and CNAP+ was 30 mm. For rat sciatic nerves, this value was 25 mm.

2.2.2 Electrical recording and stimulation

The electrical channel consists of a custom-made current-controlled stimulator and one amplifier channel. The stimulator generates biphasic square current pulses (first negative at the cathode) of 0.1-1 ms then a 10 μs delay before the recovery pulse of same duration and amplitude (ranging from 20 to 1000 μA) but opposite polarity. In experiments, the current amplitude was chosen in the plateau of the recruitment curve to ensure activation of mostly nerve fibers by the stimulus.

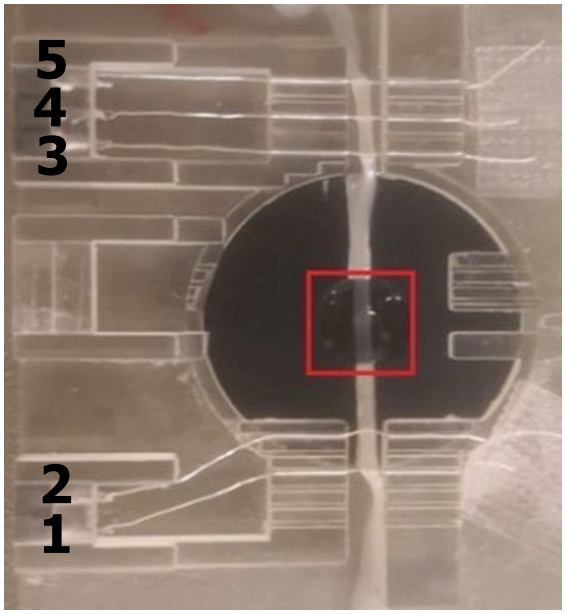

Fig. 2 Nerve chamber with the stimulation and recording electrodes placed in the grooves and a lobster nerve (first rostral leg) in the middle channel. The electrodes distribution is: 1) anode, 2) cathode, 3) GND, 4) CNAP+ and 5) CNAP-. The section of the sample illuminated and its surroundings (red box) are wet with Ringer solution.

In the recording circuit, the amplifier includes a pre-amplifier (gain: 100), an amplifier (gain: 26), an isolation stage (gain: 0.3) and a filtering stage (first-order filter), with a 10 – 8000 Hz bandwidth. This channel, when combined with the analog-to-digital converter, is characterized by a dynamic range of ± 3.46 mV with a resolution of 0.20 μV and a root-mean-square noise of 0.43 μV, all referred to the input.

2.2.3 Optical system

A schematic of the optical system is drawn in Figure 3. It was used to measure both the Stokes parameters of the light beam after propagation through the sample and the CNAP induced birefringence signal. The light source is a high-power LED emitting at 780 nm (SMB1N-780D-02, Roithner Laser Technik, Austria) powered by a stabilized current source (HP E3610A, Keysight, USA). The light beam is first collimated using an aspheric lens (25 mm diameter, 0.83 numerical aperture, effective focal length 15 mm, NIR coated, Edmund Optics, UK), it then goes through a high contrast VIS-NIR polarizer (12.5 mm diameter, Edmund Optics, UK) oriented at +45° with respect to the longitudinal axis of the nerve. A second aspheric lens (identical to the first one) focuses the polarized light on the pinhole located in the NC just beneath the sample. The optical power measured at the output of the 1 mm (0.5 mm) pinhole was ≈ 3 mW, (≈ 0.7 mW). After the nerve, the light is collected using a third aspheric lens. Afterwards, the light goes through a second polarizer,

denoted as the *analyzer*. It is oriented at -45° for measuring the CNAP induced optical change in cross-polarization configuration. A black PLA slit is placed just after the third aspheric lens to filter out unwanted reflections on the edges of the optical mounts in the setup in order to maintain a high extinction ratio ($> 1500:1$) without sample. Finally, the light is focused by a lens (LA1576-B-N-BK7, Thorlabs Inc., Germany) on a photodiode (PD). Two types of PDs were used: a S8745-01 (Hamamatsu Photonics, Japan) and a UDT-555 UV/LN (Osi Optoelectronics, USA).

The Stokes parameters of the light beam crossing the sample were measured with the same setup and without moving the sample between experiments (either CNAP recording or Stokes parameters measurements). To this end, a quarter waveplate (12.7 mm diameter, 650 – 1100 nm, Edmund Optics, UK) is inserted in the setup prior to the analyzer, and the photodiode is replaced by a high sensitivity powermeter (PM100D Thorlabs Inc., Germany).

The optical channel, housed in a metallic box, includes the photodiode (PD) in a transimpedance circuit (load resistor $R_L = 100\,k\Omega$), followed by a bandpass amplifier. This amplifier is made of a first active high pass filter of gain 101 (non-inverting configuration) with a low cut off frequency, $f_{low} = 10\,Hz$, followed by an active low pass filter (non-inverting configuration) of gain 11, with $f_{high} = 890\,Hz$ (resp. $f_{high} = 17\,kHz$) for experiments with lobster (resp. rat sciatic) nerves. Those high cut-off values were chosen according to the work of Badrenddine in lobster and mice sciatic nerves [12,26]. Because of the higher bandwidth that might be required for optical measurements in rat sciatic nerves, all experiments in these nerves were conducted with the low-noise S8745-01 photodiode. All the electronics were powered with 9 V batteries.

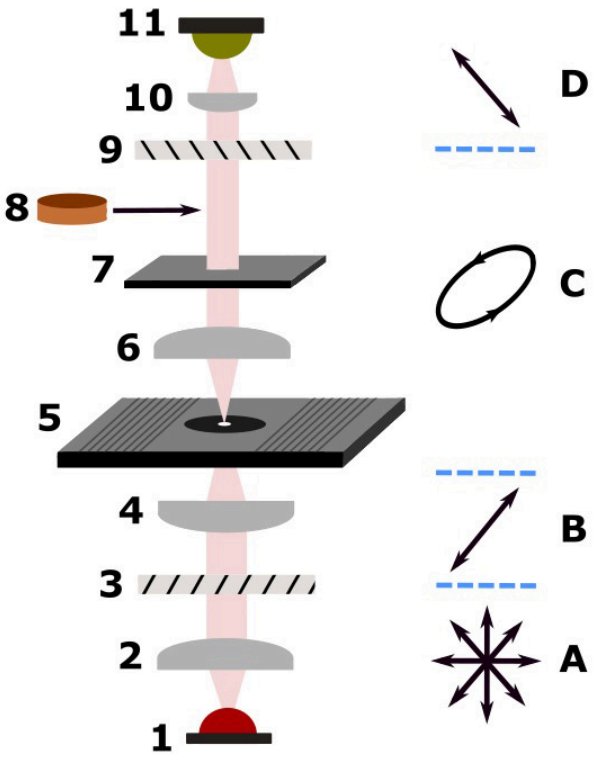

Fig. 3 Schematic of the setup. The optical components are housed in a vertical cage mount. On top, a metallic box contained the optical channel: photodiode, filters and amplifier stages. LED (1). Collimation lens (2). Polarizer (3). Focusing lens (4). Nerve chamber with the pinhole and the grooves for the electrodes (5). Collimation lens (6). Slit (7). Quarter waveplate (8) inserted in the optical system for the Stokes parameters measurement. Analyzer (9). Focusing lens (10). Photodiode (11). Unpolarized light (A). Linear polarization +45° (B). Elliptical polarization (C). Linear polarization -45° (D).

2.3 Experiment protocol

Two kinds of experiments were conducted in six lobster nerves (claws, 1st and 2nd rostral legs) and six rat sciatic nerves (main trunk of the tibialis nerve and peroneal branch). The first experiment aims to evaluate in the same nerve section, the polarization state of light transmitted during no CNAP and the birefringence signal during the CNAP propagation. The second experiments evaluates if the variation in the distribution of the nerve fibers significantly changes the output polarization state of the light. Once the nerve was dissected and adapted in the corresponding Ringer solution, it was placed in the chamber, covering the pinhole completely. The section being illuminated was wet with Marine Ringer solution, pH 7 and temperature $\approx 4°C$ (lobster) or Ringer Hepes buffered solution, pH 7.3, room tempe-rature $\approx 18 – 19°C$ (rat). Then, an electrical recruitment curve was recorded to assess its healthiness. Lobster nerves from the first and second rostral legs (thickness 0.60 – 0.90 mm), were stimulated with 1 ms biphasic current pulses. Due to their larger thickness (1.50 – 1.60 mm), lobster claw nerves were excited with 2 ms biphasic pulses. In rat sciatic nerves, 0.1 ms biphasic current pulses were applied. In the nerve two different states were defined: resting/basal (no CNAP) and dynamic (CNAP).

In the first set of experiments, the measurement of the Stokes vector and the recording of the birefringence changes were performed. To this end, the normalized Stokes parameters of the light after the nerve (for a +45° linear input polarization), denoted as S_j ($j = 0, 1, 2, 3$), were measured, following the procedure described by Schaefer [31]. Then, the cross-polarized signal in the resting state P_R is recorded during one second. Next, a train of electrical stimulation pulses is applied to the nerve to record the dynamic birefringence signal power change ΔP. Finally, the Stokes parameters were measured again to evaluate their evolution over time. During the birefringence recordings, the healthiness of the sample was

assessed by analyzing, in real time, the amplitude of the electrical CNAP. Since a visible birefringence response can be observed in single trial in each lobster nerve, only 50 excitation pulses were applied. In rat sciatic nerves, stimulation pulses were sent until there were no more evoked CNAPs or up to 500 pulses.

In the second set of experiments, the Stokes vector was measured three times at three different positions along the nerve. Before measuring the Stokes vector in a different area, two 0.1 ms electrical stimulation pulses of 1000 µA were applied to assess the healthiness of the sample.

2.4 Data processing

The outputs of the electrical and optical recording channels are digitized at 200 kHz using a DAQ (6212 USB—16 bits, National Instrument Corp., USA) and processed using MATLAB R2018 (MathWorks, Natick, USA). The birefringence signal is quantified as the ratio of the dynamic power change to the mean resting power ($\Delta P/P_R$). The amplitude of the nerve response signal (electrical and optical) is obtained by subtracting the mean base line 10 ms before the electrical stimulus onset to the peak signal amplitude. To improve the signal-to-noise ratio (SNR), a digital filter (Butterworth 3^{th} order, f_{low} = 890 Hz (lobster nerves), f_{low} = 17 kHz or 890 Hz (rat sciatic nerves) was applied to the raw data. For measurements in rat SNs, this was followed by signal averaging over the whole excitation sequence (i.e., up to max 500 stimulation pulses).

3 STOKES-MUELLER ANALYSIS

3.1 Modeling of the optical signal

Nerve fibers can basically be considered as long cylinders with cytoskeletal components such as microtubules and neurofilaments oriented along the longitudinal axis, with a membrane made of proteins and lipid molecules oriented radially [26]. Because of this structure, the optical properties are different for light polarized along the nerve longitudinal axis or in the transverse plane [33]. This anisotropy gives rise to birefringence and diattenuation [34]. Moreover, the scattering experienced by light when propagating in the nerve could lead to light depolarization, a phenomenon by which an incident beam, initially fully polarized, becomes partially polarized or even totally unpolarized.

Within the Stokes formalism for representing (partially) polarized light, Muller matrices are used to model the change of the polarization state between the input and the output of an optical system [35]. Besides, a Muller matrix can be decomposed into the product of three Muller matrices that have a direct physical meaning, namely a depolarizer ($\mathbf{M}_\Delta$), a retarder ($\mathbf{M}_R$) and a diattenuator ($\mathbf{M}_D$) [36]. The polarization state of a beam at the output of an arbitrary depolarizing optical system, such as a biological sample, can thus be written as [36,37]:

$$\mathbf{S}_{out} = \mathbf{M}\mathbf{S}_{in} = \mathbf{M}_\Delta \mathbf{M}_R \mathbf{M}_D \mathbf{S}_{in}, \quad (1)$$

where $\mathbf{M}$ is the Muller matrix of the sample and $\mathbf{S}_{in,out}$ are the Stokes vectors of the input and output beams.

Considering more specifically light propagation in nerves and with the aim of deriving a model for the optical signal in the resting and in the dynamic states, the matrices in Eq. 1 can reasonably be simplified. First, since nerves are turbid media, light experiences multiple scattering when propagating in the nerve, which is known to lead to depolarization [38,39].To the extent of our knowledge, polarizance values of neural tissues have not been reported in the literature. Nevertheless, it has been shown in complex tissue structures, such as the colon [40] or prostate [41], that the polarizance is close to zero. In the context of this work, no polarizance is considered and a uniform depolarization is thus assumed. This depolarization results in an output degree of polarization DOP < 1. Secondly, owing to its specific structure, the nerve will be considered as a linearly birefringent medium of retardance φ_R, with one of the two polarization eigenmodes oriented along the nerve axis [10,24]. In this regard, the thickness of the nerve is assumed to be uniform across the beam. Lastly, diattenuation is neglected because it is low and has only a small impact on polarization in biological media [42,43]. With these assumptions, Eq. 1 reads:

$$\mathbf{S}_{out} = \begin{pmatrix} 1 & \vec{0}^T \\ \vec{0} & \mathrm{DOP}\mathbf{I}_3 \end{pmatrix} \begin{pmatrix} 1 & \vec{0}^T \\ \vec{0} & \mathbf{m}_R \end{pmatrix} T_u \mathbf{S}_{in}, \quad (2)$$

where T_u is the transmittance through the sample for fully unpolarized light, $\mathbf{I}_3$ is the 3×3 identity matrix and $\mathbf{m}_R$ is the 3×3 rotation matrix of angle φ_R around the axis $(1\ 0\ 0)^T$.

3.2 Polarization and optical signal in the resting state

For an incident beam of power P_{in}, linearly polarized at +45° with respect to the nerve axis, $\mathbf{S}_{in} = P_{in}(1\ 0\ 1\ 0)^T$, which gives:

$$\mathbf{S}_{out} = T_u P_{in} \left(1\ \ 0\ \ \mathrm{DOP}\cos[\varphi_R]\ \ \mathrm{DOP}\sin[\varphi_R]\right)^T. \quad (3)$$

In the resting state, the retardance keeps by definition a constant value. After the analyzer (linear polarizer oriented at –45°), the power P_R reaching the photodiode reads:

$$P_R = \beta \mathbf{M}_{-45°} \mathbf{S}_{out} = \beta \frac{T_u P_{in}}{2} \left(1 - \mathrm{DOP}\cos[\varphi_R]\right), \quad (4)$$

where $\mathbf{M}_{-45°}$ is the Muller matrix of the linear polarizer and β is the fraction of the output power that reaches the photodiode due to the limited aperture of the analyzer.

3.3 Optical signal in the dynamic state

When nerves are electrically excited, a change of birefringence, dichroism, absorbance and scattering might arise [19,44]. Each of these phenomena affects the output polarization state in a different way and could contribute to a transient change in the measured optical signal after the analyzer. In crab leg nerves and squid axons, the cross-polarized signal in the dynamic state arises almost entirely from a change in linear retardance close to the axon membrane, with little or no contribution from scattering, absorption, linear dichroism or optical activity [24]. The change of absorption or turbidity in lobster nerves in the dynamic state has a negligible contribution to the birefringence signal [44]. In addition, the optical activity variation (circular birefringence), while not always negligible, remains smaller than the linear retardance variation [44]. Moreover, since the birefringence change is much smaller than the resting birefringence, the polarization eigenmodes can be assumed to be identical in the resting and the dynamic states, in agreement with results showing that the cross-polarized signal is maximized when the sample is aligned at 45° with respect to the two polarizers [10,24]. Consequently, in the following we will restrict the optical changes in the dynamic state to the dynamic variation of the retardance $\Delta\varphi$. From Eq. 1, the polarization state at the output of the nerve in its dynamic state is then:

$$\mathbf{S}_{\text{out,d}} = \mathbf{M}_{\Delta}\left(\mathbf{M}_{\text{R}} + \frac{\text{d}\mathbf{M}_{\text{R}}}{\text{d}\varphi_{\text{R}}}\Delta\varphi\right)\mathbf{M}_{\text{D}}\mathbf{S}_{\text{in}}. \tag{5}$$

It follows that the power variation in the dynamic state ΔP, measured through the analyzer is given by:

$$\Delta\text{P} = \beta\frac{\text{T}_{\text{u}}\text{P}_{\text{in}}}{2}\text{DOP}\sin\left(\varphi_{\text{R}}\right)\Delta\varphi. \tag{6}$$

As can be seen, ΔP does not only depend on the retardance variation and the incident power but also on the degree of polarization of the beam at the nerve output (DOP). To some extent, a decrease of the DOP due to scattering in the sample could therefore be compensated by an increase of the incident power to maintain the signal-to-noise ratio in the measured optical signal.

3.4 Signal-to-noise-ratio

We will now look at the signal-to-noise ratio (SNR) of the transient optical signal measured in the dynamic state. The light source, the shot noise and the thermal noise generated in the detector each contribute to the noise. The total voltage noise variance at the detector output and after the bandpass amplifier is thus:

$$\sigma_{\text{tot}}^2 = \sigma_{\text{th}}^2 + \sigma_{\text{I}}^2 + \sigma_{\text{s}}^2, \tag{7}$$

where σ_{th} is the RMS of the thermal noise generated by the electronics in the detector (load resistors and amplifier stages) and σ_{I} is the RMS of the amplitude noise of the light source. Since the source is a LED, this optical noise is dominated in the bandwidth of the detector Δf, by the 1/f noise [45] . σ_{s} is the RMS of the shot noise characterizing quantum fluctuations of detected photons. With R, the responsivity of the photodiode at the LED wavelength, q, the elementary charge, R_{L}, the load resistor in the transimpedance front end of the detector and G, the gain of the bandpass amplifier, the shot noise RMS reads:

$$\sigma_{\text{s}} = \text{R}_{\text{L}}\text{G}\sqrt{2\text{qRP}_{\text{R}}(\pi/2)\Delta_{\text{f}}}, \tag{8}$$

where $\pi/2$ is a correction factor for the first-order filters in the detector. We note that when the retardance in the sample is not compensated before the analyzer or when the scattering depolarizes the output beam, the power in the resting state quickly rises which, in turn, increases the shot noise. As a result, with the typical power level measured in the resting state with our setup (about 34 μW), the noise is dominated by the shot noise. The voltage signal due to the CNAP induced optical change, measured at the output of the bandpass amplifier is:

$$\text{V}_{\text{out}} = \text{R}_{\text{L}}\text{GR}\Delta\text{P}. \tag{9}$$

The signal-to-noise ratio (SNR) of the voltage signal is defined as the ratio between the signal power and the noise power. Assuming that the main contribution to the noise is the shot noise, by using Eqs.4, 6, 8 and 9, the SNR of the signal, recorded during the CNAP propagation, is:

$$\text{SNR} = \frac{\beta\text{T}_{\text{u}}\text{R}}{2\text{q}\pi\Delta_{\text{f}}}\frac{\text{P}_{\text{in}}\text{DOP}^2\sin\left(\varphi_{\text{R}}\right)^2\Delta\varphi^2}{1-\text{DOP}\cos\left(\varphi_{\text{R}}\right)}. \tag{10}$$

4 RESULTS

4.1 Lobster nerves

All crustacean nerves (S01-S06) produced clear electrical and optical traces for single-trial CNAPs. The amplitude of the electrical signal was in the range 84 – 913 μV. The RMS voltage of the noise, measured at the output of the optical channel, was dominated by the shot noise in all these experiments. In the dynamic state, the change in optical signal normalized to the res-ting signal ($\Delta\text{P}/\text{P}_{\text{R}}$) was in the range $2\times10^{-5} - 1.7\times10^{-4}$, while the SNR varied from 14 to 32 dB. A typical example, recorded in sample S01, is reported in Figure 4. In the resting state, the measured RMS noise in the optical channel was $\approx$ 8.8 mVrms (Figure 4A). In this experiment, the power reaching the sensor was $\approx$ 34 μW, for an incident power on sample P_{in} = 3 mW (1 mm pinhole), leading to a theoretical shot noise of $\approx$ 8.2 mVrms, in agreement with the measured voltage signals with and without light. Electrical and optical traces for single-trial CNAPs are shown in Figures 4B-C.

Measurements of the Stokes parameters show that the light transmitted through the nerve is only slightly depolarized due to scattering, with DOP values ranging from 0.92 to 1.00 (see Figure 5A). For nerve thicknesses below 1 mm, the depolarization was quite small but became noticeable for larger nerve diameters, such as for claw's nerves. Besides, we observed only little variations of the DOP across the neural tissue. We can also see that the S1 component remains small ($\approx$ –0.1 [46]) and, considering different nerve thicknesses, that the polarized part of the output Stokes vector mainly undergoes a rotation in the S2-S3 plane. The rotation angle shows, in most samples, a linear relation with the sample thickness corresponding to a retardance of ≈ 0.75 rad/mm. We note that the systematic nonzero value S_1 could be the result of a slight misalignment of the polarizers and waveplates. However, the total power measured in the bases (0°,90°) and (–45°,+45°) agree within 1%. Nevertheless, this does not affect much the DOP or the measured retardance, nor the general conclusion of our work.

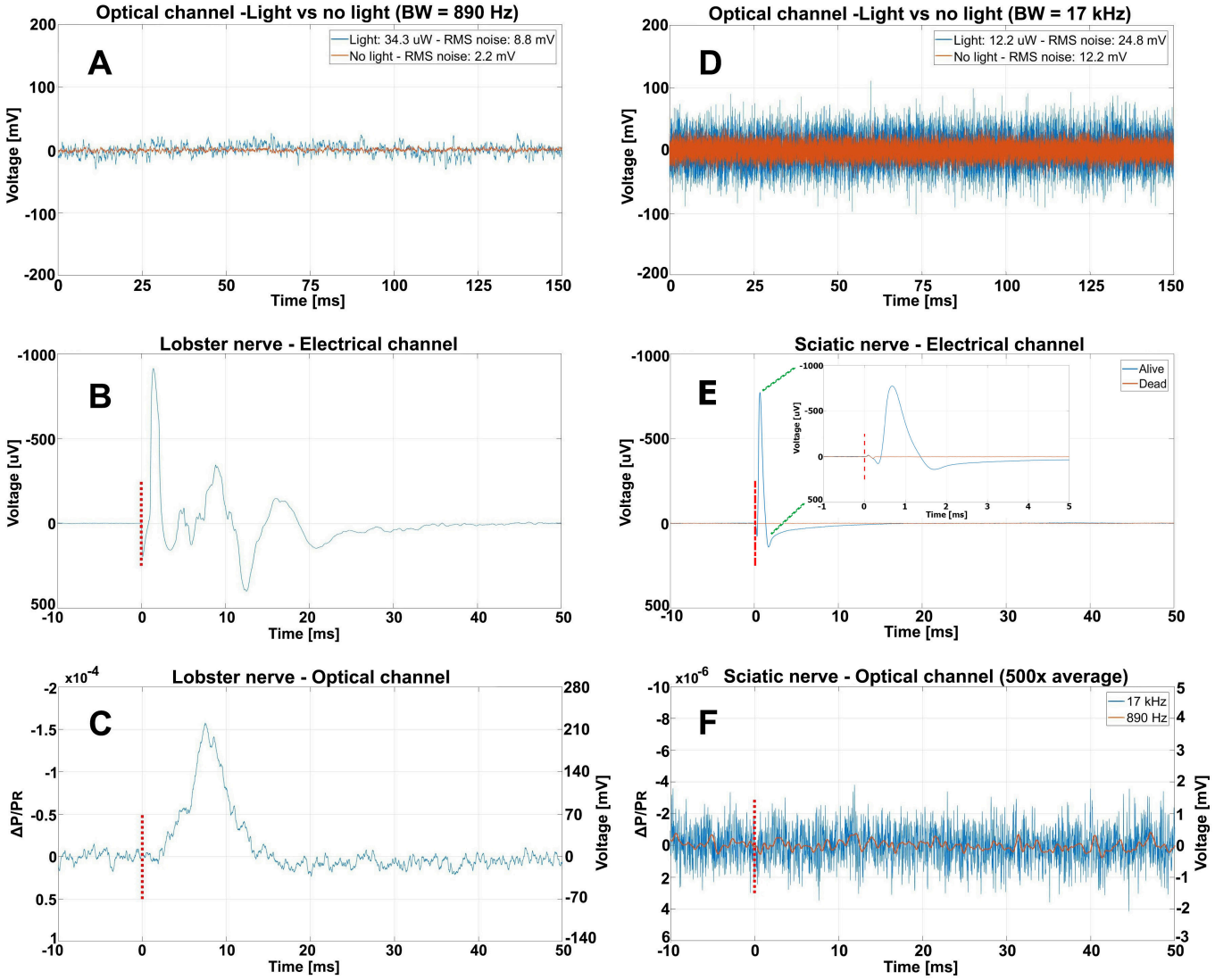

Fig. 4 Typical electrical and optical recordings in lobster walking leg nerves (left column, S01) and rat sciatic nerves (right column, S14). Both samples exhibited similar thickness ($\approx$ 0.9 mm). (A) and (D) signal recorded at the output of the optical channel, without and with incident light in the resting state, showing shot noise limited measurements in both experiments. The power reaching the photodiode is $\approx$ 34 µW and $\approx$ 12 µW, respectively. (B) and (E) Electrical CNAPs. The voltage amplitude refers to the input of the electrical channel. (C) and (F), recordings in the optical channel. A raw single trace is shown for the experiment in lobster nerve, while an average over 500 trials is displayed for rat SN. Despite numerical filtering (890 Hz bandwidth and averaging), no birefringence signal can be seen.

In the dynamic state, from the signal acquired in the optical channel and using Eq. 6, the computed peak value of the retardance variation $\Delta\varphi$ was measured to be in the range 13 – 57 μrad (i.e ≈ 1.6 – 7 pm).

4.2 Rat sciatic nerves

In rat sciatic nerves (main trunk S13 – S15 and peroneal branch S19 – S21), electrical single-trial CNAPs were recorded with amplitudes ranging from 500 to 3000 μV. Yet, no optical response was detected, even after a numerical post-processing consisting in averaging up to 500 traces and in further filtering the signal (890 Hz bandwidth). As an illustration, signals recorded from nerve S14 are shown in Figures 4E-F. We note that despite the larger bandwidth of the receiver (17 kHz), the RMS total voltage noise was still limited by the shot noise (see Figure 4D). The power reaching the photodiode was ≈ 12 μW for an incident power on sample P_{in} = 3 mW (1 mm pinhole), leading to a theoretical shot noise of ≈ 21 mVrms, in agreement with the measured voltage signals with and without light. Light transmitted through the main trunk of the nerve in different areas, exhibited an almost complete depolarization due to scattering. In the peroneal branch (S19-S24, thickness ≈ 0.5 mm), the DOP was measured to be in the range 0.10 – 0.12, while it drops to zero (within the measurement uncertainties) for a thicker portion of the nerve in the main trunk (S13-S18, thickness ≈ 1 mm). This is also seen in Figure 5B, with the Stokes parameters $S_{1,2,3}$ close to zero. Because of the measurement variability, it was not possible to infer a retardance value per unit of sample thickness.

Cross-polarized images of the peroneal branch oriented at 45° and aligned with the axes of the polarizers are shown in Figure 6. They were acquired with our experimental setup by replacing the photodiode with a microscope objective (NA=0.42) and a CMOS camera, as well as the sample holder with a glass plate. The pinhole and the slit were also removed. As can be seen, there is no significant difference with the nerve orientation, except near the edge where the sample is thinner, confirming the strong light depolarization in the central part of the nerve. Moreover, contrary to experiments in very thin neural samples [26,47–49], individual axons cannot be seen despite their strong birefringence because of a lack of contrast due to the averaging effect over many axons and to blurring from light scattering.

5 DISCUSSION

Most biological tissues are complex turbid media. Their optical properties are mainly characterized by absorption and scattering, both being wavelength dependent [32]. Scattering, which is the consequence of the inhomogeneous distribution of the

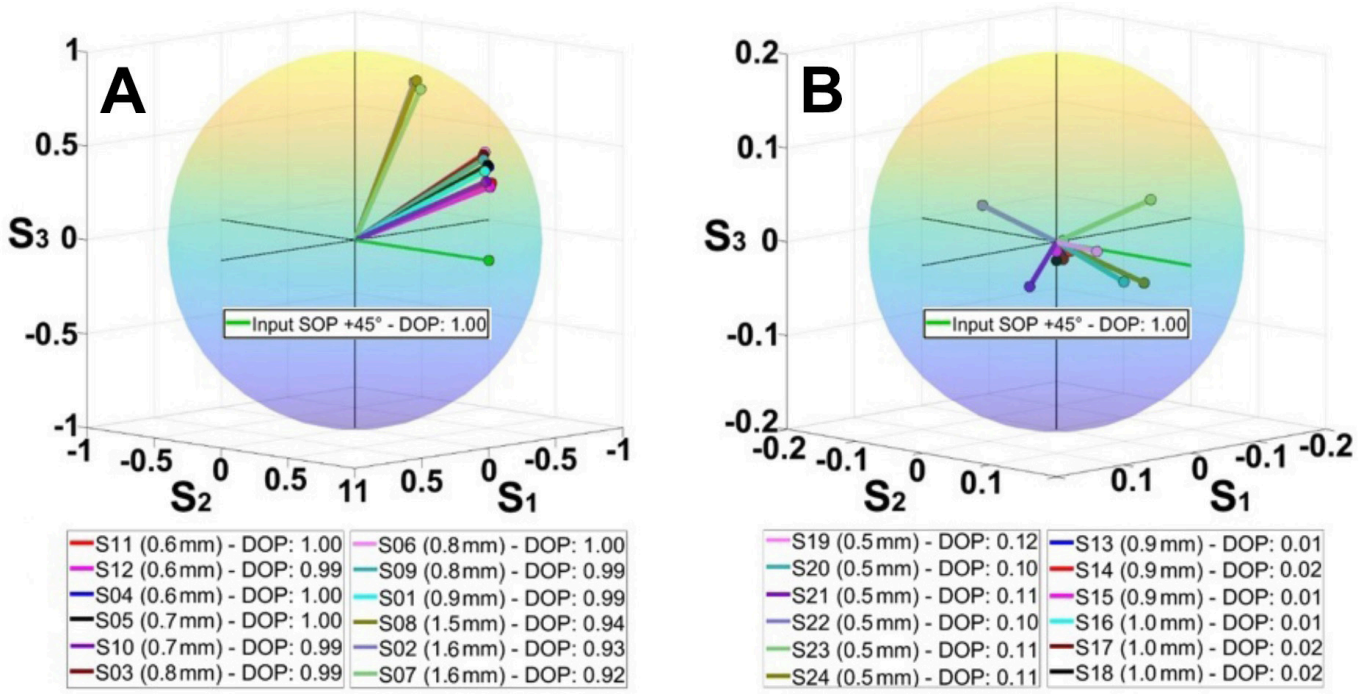

Fig. 5 Stokes vectors representation on the Poincaré sphere for experiments conducted in lobster (A) and rat sciatic (B) nerves. The incident light on sample is linearly polarized at +45° with DOP=1.00 (green vector). The color labels in (A) and (B) are organized based on the nerve diameter, from the thinnest to the thickest. The Stokes parameters for all samples (S_j) are reported in the supporting information [46]).

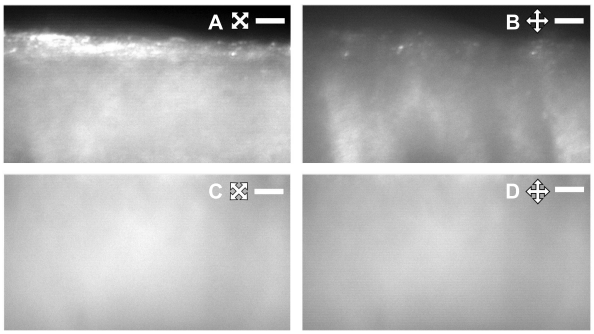

Fig. 6 Cross-polarized images of the peroneal branch of a rat sciatic nerve. The sample is oriented at 45° (A–C) or aligned (B–D) with the axes of the polarizers. The scale bar corresponds to 50 μm and the cross represents the orientation of the polarizer and the analyzer. A–B: Edge of the nerve, the average brightness in B is ≈ 24% smaller than in A. C–D: Central part of the nerve, the average brightness in D is ≈ 11% smaller than in C.

refractive index [33], decreases monotonically with wavelength in biological structures. Light thus experiences a larger penetration depth in the NIR than in the visible absorption bands. We have thus chosen a light source at 780 nm which is close to an absorption minimum by water in the NIR spectrum because scattering decreases with wavelength and because larger birefringence signals in the NIR than in the visible range have been reported [23].

When absorption is negligible, the transport mean free path (TMFP) coincides with the distance over which photons have lost their initial direction of propagation. It is then given by TMFP=$1/\mu_s'$, where μ_s' is the reduced scattering coefficient. In studies conducted in rat and human brains, TMFP values were reported in the range [1–2] mm [50], as well as [0.12–0.6] mm [51–53]. These differences can be explained by the fact that the density of components in the tissue such as myelin, cell bodies or neurites are varying along the brain structure. Considering that rat sciatic nerves have a similar constitution than brain, the TMFP could thus be smaller than their diameter.

In addition to reducing the transmitted power, scattering also leads to depolarization. It has been shown by Xu and Alfano that the light isotropization and linear depolarization occur on the same characteristic length [38]. Moreover, they showed that this length is greater than the TMFP and, for large Mie scatterers, is of the order of 1–1.5×TMFP.

In our experiments on rat sciatic nerves, we reported evidence of a high linear depolarization for > 0.5 mm thick sections. In stark contrast, the light remains almost fully polarized in crustacean nerves, even for thicknesses larger than 1.5 mm. This noticeable differences between lobster and rat sciatic nerves can be related to their respective structures. A lobster nerve comprises ≈ 1000 unmyelinated axons with diameters ranging from 1 to 100 μm [27]. In rat sciatic nerves, the main trunk contains ≈ 27 000 axons (30 % myelinated and 70 % unmyelinated) with diameters spanning 0.1 – 1 μm (unmyelinated) and 1 – 14 μm (myelinated) [28].

Nerve fibers have a structural anisotropy that results in an intrinsic birefringence [12,34,43]. In order to have an analytical expression of the expected SNR of the birefringence signal, we considered the propagation through the nerve section as in linear birefringent media to account for the polarization change. This model is supported by several indicators. Early works on birefringence nerve properties, demonstrated, for crab leg nerves and squid axons, that it is relevant to quantify the average retardation as if these nerves behave like uniaxial birefringent media with an effective optic axis longitudinally oriented [24]. This was confirmed for lobster nerves in our experiments. We indeed measured a polarization rotation (around the S_1 axis) proportional to the sample thickness (see Figure 5A). The resulting resting retardances are in line with previously reported values [44]. In rat sciatic nerves, it was however not possible to verify the model due to the high measurement variability. This can be explained by the more complex and inhomogeneous structure of these nerves. Nevertheless, thinner samples under a polarizing microscope have revealed that myelinated nerve axons are birefringent media [25,43,47,47–49]. In particular, the myelin sheath, with its concentric layer structure, exhibits strong linear birefringence with a radially oriented optic axis. As a result, it is expected that only the sides of each axon sheath to contribute to the resting linear birefringence for light propagating orthogonally to the nerve section. However, axons in peripheral nerve fibers do not follow a straight line but instead show an undulating course of variable wavelength and amplitude [55]. This contributes to increasing the depolarization of the whole light beam but could also modify the orientation of the effective optic axis, explaining the variability in our measurements.

We now consider the signal resulting from a change in optical retardation accompanying the propagation of CNAPs along the nerves. Optical single trials measurements in lobster nerves were obtained successfully. The measured retardance variations, in the range [1.6–7] pm, have an amplitude comparable to results of previous works in similar specimens [56,57]. Figure 7A shows the theoretical signal-to-noise ratio of the birefringence signal with the DOP (Eq. 10) in lobster nerves for various input powers, considering our experimental parameters for the sample S03. In this sample, for an input power of 3 mW, the SNR reached 32 dB in very good agreement with our model. We see also from these curves that a few milliwatts input power are sufficient to reach a SNR$>$ 10 dB, even for DOPs as small as 0.3.

The absence of detectable birefringence signals in experiments with rat sciatic nerves, even when a digital filter with a 890 Hz bandwidth is applied, could at first sight be explained by the scattering of light resulting from the higher number of

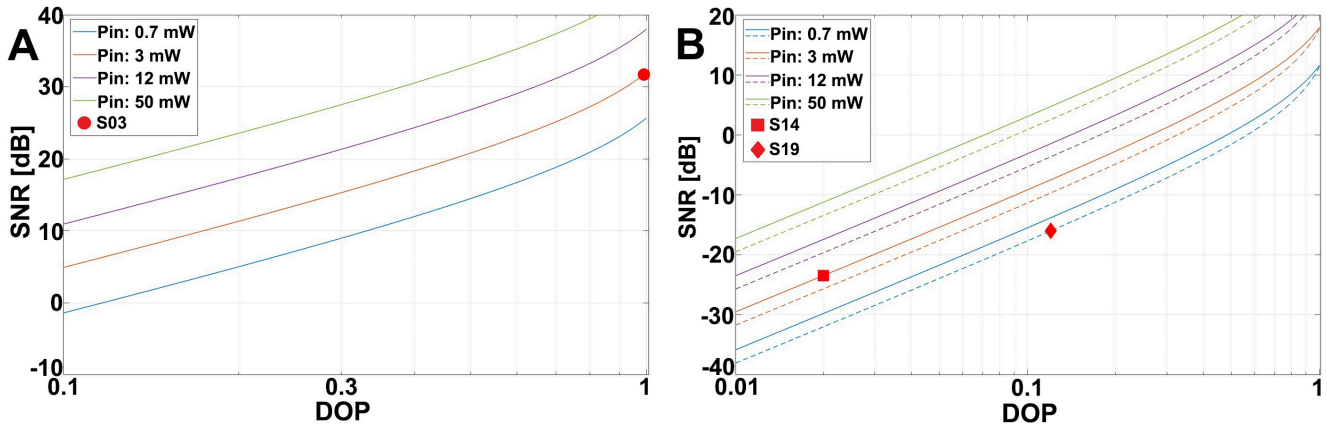

Fig. 7 Variation of the SNR with the DOP for several optical powers (P_{in}) from Eq. 10, with parameters corresponding to our experiments with lobster and rat sciatic nerves. The receiver bandwidth is 890 Hz. A) Lobster (S03). The sample exhibited $\varphi_R \approx 0.6$ rad, $\Delta\varphi \approx 57\,\mu$rad, DOP ≈ 0.99 and $\beta T_u \approx 0.19$ (P_{in}=3 mW, $P_{out} \approx 570\,\mu$W). B) Rat (main nerve trunk S14 and peroneal branch S19). For the main trunk (solid): DOP ≈ 0.02 and $\beta T_u \approx 0.008$ (P_{in} = 3 mW, $P_{out} \approx 25\,\mu$W); for the peroneal branch (dashed): DOP ≈ 0.12 and $\beta T_u \approx 0.015$ (P_{in}=0.7 mW, $P_{out} \approx 10\,\mu$W). In these plots, we assumed a resting retardance and a retardance variation corresponding to lobster nerves of similar thickness, i.e. in the main trunk $\varphi_R = 0.6$ rad, $\Delta\varphi = 57\,\mu$rad and in the peroneal branch $\varphi_R = 0.48$ rad, $\Delta\varphi = 40\,\mu$rad. We note that despite the smaller βT_u coefficient, the SNR is expected to be slightly larger in the main trunk because of a higher φ_R and $\Delta\varphi$. The red dot in A) indicates the experimental SNR, while the red marks in B) show the theoretical SNR with the corresponding experimental parameters.

(small) axons and the myelin sheaths [23]. As discussed earlier, this indeed reduces the DOP as well as the power reaching the detector (i.e. the product βT_u). In the peroneal branch of the nerve where the thickness is about 0.5 mm, we typically measured a DOP and a βT_u factor about 10 times lower than in 1 mm-thick crustacean nerves. This leads to an expected SNR of -16 dB assuming that all the other parameters, such as the resting birefringence and dynamical retardance, are identical to lobster nerves of similar thicknesses (see Figure 7B). The situation is even worse for 1 mm thick sections in the main trunk for which a theoretical SNR of -24 dB is predicted. We stress that in the model as well as in the experiments (see Figure 4D) the main source of noise is the shot noise. Increasing the power up to 50 mW should still not be sufficient for single trial measurements. A detectable birefringence signal could in principle be obtained by averaging on successive nerve excitations. Yet, no signal can be seen when averaging 500 dynamic traces recorded in the main and peroneal branches, while in this case our model predicts a SNR about 3 dB and 11 dB, respectively. This led us to conclude that the retardance variation itself is much smaller than assumed (by at least one order of magnitude), since our experimental results cannot be explained only by the decrease of the DOP and of the transmission due to tissue scattering properties.

It is now accepted that the retardance changes occur close to or through the axon membrane and are associated with membrane depolarization [12,19,24]. Moreover, it has been shown in squid giant axons that the birefringent signal in the dynamic state is consistent with the reorientation of peptide bonds in voltage gated sodium channels [58]. In addition, it could find its origin in conformational changes in the membrane and its surroundings due to the large local electric field (10^7 V/m) during the CNAP propagation [59]. While the mechanism behind birefringence variation is still an open question, we hypothesize that in myelinated axons in peripheral nerves, the birefringence changes only take place at the nodes of Ranvier. During saltatory conduction, the membrane depolarization remains localized at these nodes where the density of sodium channels is high [60]. However, despite the higher channel concentration, since the nodes have a small size ($\approx$ 1–2 μm) and are separated by up to $\approx$ 1.5 mm, the overall signal from excited myelinated axons remains low and hiders the buildup of a large birefringent signal. We note that even if the majority of axons in the mid-tight and peroneal branch of rat sciatic nerves are unmyelinated, they are characterized by a large stimulation threshold (above 10 times than myelinated axons [54]). This means that they are hardly excitable with traditional electrical stimulation settings as in this work. This is in agreement with OCT imaging of neural activity in rat sciatic nerves in which no retardance variations has been observed despite evidence of light scattering changes due to osmotic swelling from ion currents in the dynamic state [22].

In conclusion, we showed that the cross-polarized technique in transmission is unsuitable for monitoring CNAPs in sciatic nerves (0.5 mm thick and above). This is attributable not only to higher scattering of photons that drastically reduces the degree of polarization of the transmitted light and the transmission itself, but also to an intrinsic smaller birefringence change. Both detrimental effects find their origin in the myelin sheaths. In the context of clinical applications, while

techniques relying on scattering changes seem more appropriate than those based on birefringence changes for sciatic nerves, the latter method could still be promising for nerves containing less myelinated axons. It is the case, for instance, for the vagus nerve, showing a specific clinical interest in epilepsy [61]. To which extend polarization techniques could be implemented for monitoring neural activity in vagus nerves remains an open question and requires further investigations.

Acknowledgments

The research was supported by the Walloon Region, Belgium—Pole Mecatech (Project NEUROPV n7740). We are grateful for the help provided by Geoffrey Vanbienne in the realisation of our electronic setup.

Conflict of interest

Antoine Nonclercq is member of the scientific committee of Synergia Medical. Besides this, the authors have no conflicts of interest to declare.

References

1 Vonck, K., Boon, P., Goossens, L., Dedeurwaerdere, S., Claeys, P., Gossiaux, F., ... Williamson, P. (2003). Neurostimulation for refractory epilepsy. Acta neurologica belgica, 103(4), 212-217.

2 Mekhail, N. A., Aeschbach, A., Stanton-Hicks, M. (2004). Cost benefit analysis of neurostimulation for chronic pain. The Clinical journal of pain, 20(6), 462-468.

3 Deuschl, G., Agid, Y. (2013). Subthalamic neurostimulation for Parkinson's disease with early fluctuations: balancing the risks and benefits. The Lancet Neurology, 12(10), 1025-1034.

4 Marangell, L. B., Martinez, M., Jurdi, R. A., Zboyan, H. (2007). Neurostimulation therapies in depression: a review of new modalities. Acta Psychiatrica Scandinavica, 116(3), 174-181.

5 Patrick, A. Epstein, O. Review article: Gastroparesis. Aliment. Pharmacol. Ther. 27, 724–740 (2008).

6 Herzog, J., Hamel, W., Wenzelburger, R., Pötter, M., Pinsker, M. O., Bartussek, J., ... Volkmann, J. (2007). Kinematic analysis of thalamic versus subthalamic neurostimulation in postural and intention tremor. Brain, 130(6), 1608-1625.

7 Ruiz-Tovar, J., Oller, I., Diez, M., Zubiaga, L., Arroyo, A., Calpena, R. (2014). Percutaneous electrical neurostimulation of dermatome T6 for appetite reduction and weight loss in morbidly obese patients. Obesity surgery, 24(2), 205-211.

8 Popeney, C. A., Aló, K. M. (2003). Peripheral neurostimulation for the treatment of chronic, disabling transformed migraine. Headache: The Journal of Head and Face Pain, 43(4), 369-375.

9 De Ferrari, G. M., Crijns, H. J., Borggrefe, M., Milasinovic, G., Smid, J., Zabel, M., ... Schwartz, P. J. (2011). Chronic vagus nerve stimulation: a new and promising therapeutic approach for chronic heart failure. European heart journal, 32(7), 847-855.

10 Yao, X. C., Foust, A., Rector, D. M., Barrowes, B., George, J. S. (2005). Cross-polarized reflected light measurement of fast optical responses associated with neural activation. Biophysical journal, 88(6), 4170-4177.

11 Gulino, M., Kim, D., Pané, S., Santos, S. D., Pêgo, A. P. (2019). Tissue response to neural implants: the use of model systems toward new design solutions of implantable microelectrodes. Frontiers in neuroscience, 13, 689.

12 Badreddine, A. H., Schoener, K. J., Bigio, I. J. (2015). Elucidating the temporal dynamics of optical birefringence changes in crustacean nerves. Biomedical optics express, 6(10), 4165-4178.

13 Dautrebande, M., Doguet, P., Gorza, S. P., Delbeke, J., Nonclercq, A. (2018). Peripheral nerve recruitment curve using near-infrared stimulation. In Optogenetics and Optical Manipulation 2018 (Vol. 10482, p. 104820V). International Society for Optics and Photonics.

14 Zecevic, D., Antic, S. (1998). Fast optical measurement of membrane potential changes at multiple sites on an individual nerve cell. The Histochemical Journal, 30(3), 197-216.

15 Peterka, D. S., Takahashi, H., Yuste, R. (2011). Imaging voltage in neurons. Neuron, 69(1), 9-21.

16 Kralj, J. M., Douglass, A. D., Hochbaum, D. R., Maclaurin, D., Cohen, A. E. (2012). Optical recording of action potentials in mammalian neurons using a microbial rhodopsin. Nature methods, 9(1), 90-95.

17 Dombeck, D. A., Blanchard-Desce, M., Webb, W. W. (2004). Optical recording of action potentials with second-harmonic generation microscopy. Journal of Neuroscience, 24(4), 999-1003.

18 Stepnoski, R. A., LaPorta, A., Raccuia-Behling, F., Blonder, G. E., Slusher, R. E., Kleinfeld, D. (1991). Noninvasive detection of changes in membrane potential in cultured neurons by light scattering. Proceedings of the National Academy of Sciences, 88(21), 9382-9386.

19 Carter, K. M., George, J. S., Rector, D. M. (2004). Simultaneous birefringence and scattered light measurements reveal anatomical features in isolated crustacean nerve. Journal of neuroscience methods, 135(1-2), 9-16.

20 Sherebrin, M. H. (1972). Changes in infrared spectrum of nerve during excitation. Nature New Biology, 235(56), 122-124.

21 Laporta, A. Kleinfeld, D. Interferometric detection of action potentials. Cold Spring Harb. Protoc. 7, 307–311 (2012).

22 Hope, J., Goodwin, M., Vanholsbeeck, F. (2021). Optical coherence tomography imaging of evoked neural activity in sciatic nerve of rat. Journal of Physics D: Applied Physics, 54(33), 334002.

23 Foust, A. J., Beiu, R. M., Rector, D. M. (2005). Optimized birefringence changes during isolated nerve activation. Applied optics, 44(11), 2008-2012.

24 Cohen, L. B., Hille, B., Keynes, R. D. (1970). Changes in axon birefringence during the action potential. The Journal of physiol-

ogy, 211(2), 495-515.

25 Koike-Tani, M., Tominaga, T., Oldenbourg, R., Tani, T. (2020). Birefringence changes of dendrites in mouse hippocampal slices revealed with polarizing microscopy. Biophysical journal, 118(10), 2366-2384.

26 Badreddine, A.H., Optical tracking of nerve activity using intrinsic changes in birefringence. 2017, Boston University.

27 De Lorenzo, A. D., Brzin, M., Dettbarn, W. D. (1968). Fine structure and organization of nerve fibers and giant axons in Homarus americanus. Journal of ultrastructure research, 24(5-6), 367-384.

28 Žužek, M. C., Rozman, J., Pečlin, P., Vrecl, M., Frangež, R. (2017). Analysis of compound action potentials elicited with specific current stimulating pulses in an isolated rat sciatic nerve. Biomedical Engineering/Biomedizinische Technik, 62(1), 37-48.

29 Furusawa, K. (1929). The depolarization of crustacean nerve by stimulation or oxygen want. The Journal of physiology, 67(4), 325.

30 Cury, J., Perre, L. V., Smets, H., Stumpp, L., Vespa, S., Vanhoestenberghe, A., ... Nonclercq, A. (2021). Infrared neurostimulation in ex-vivo rat sciatic nerve using 1470 nm wavelength. Journal of neural engineering, 18(5), 056018.

31 Schaefer, B., Collett, E., Smyth, R., Barrett, D., Fraher, B. (2007). Measuring the Stokes polarization parameters. American Journal of Physics, 75(2), 163-168.

32 Fanjul-Vélez, F., Arce-Diego, J. L. (2011, April). Light propagation in turbid media: Application to biological tissues. In Proceedings of 21st International Conference Radioelektronika 2011 (pp. 1-4). IEEE.

33 Tuchin, V. V. (2016). Polarized light interaction with tissues. Journal of biomedical optics, 21(7), 071114.

34 Mehta, S. B., Shribak, M., Oldenbourg, R. (2013). Polarized light imaging of birefringence and diattenuation at high resolution and high sensitivity. Journal of Optics, 15(9), 094007.

35 González de Sande, J. C., Santarsiero, M. (2017). Mueller matrix polarimetry by means of azimuthally polarized beams and adapted commercial polarimeter.

36 Lu, S. Y., Chipman, R. A. (1996). Interpretation of Mueller matrices based on polar decomposition. JOSA A, 13(5), 1106-1113.

37 Ossikovski, R., De Martino, A., Guyot, S. (2007). Forward and reverse product decompositions of depolarizing Mueller matrices. Optics letters, 32(6), 689-691.

38 Xu, M., Alfano, R. R. (2005). Random walk of polarized light in turbid media. Physical review letters, 95(21), 213901.

39 Bicout, D., Brosseau, C., Martinez, A. S., Schmitt, J. M. (1994). Depolarization of multiply scattered waves by spherical diffusers: Influence of the size parameter. Physical Review E, 49(2), 1767.

40 Ivanov, D., Dremin, V., Borisova, E., Bykov, A., Novikova, T., Meglinski, I., Ossikovski, R. (2021). Polarization and depolarization metrics as optical markers in support to histopathology of ex vivo colon tissue. Biomedical Optics Express, 12(7), 4560-4572.

41 Badieyan, S., Ameri, A., Razzaghi, M. R., Rafii-Tabar, H., Sasanpour, P. (2019). Mueller matrix imaging of prostate bulk tissues; Polarization parameters as a discriminating benchmark. Photodiagnosis and photodynamic therapy, 26, 90-96.

42 Chue-Sang, J., Gonzalez, M., Pierre, A., Laughrey, M., Saytashev, I., Novikova, T., Ramella-Roman, J. C. (2019). Optical phantoms for biomedical polarimetry: a review. Journal of biomedical optics, 24(3), 030901.

43 Menzel, M., Reckfort, J., Weigand, D., Köse, H., Amunts, K., Axer, M. (2017). Diattenuation of brain tissue and its impact on 3D polarized light imaging. Biomedical optics express, 8(7), 3163.

44 Watanabe, (1987). Change in optical activity of a lobster nerve associated with excitation. The Journal of physiology, 389(1), 223-253.

45 Rumyantsev, S. L., Sawyer, S., Pala, N., Shur, M. S., Bilenko, Y., Zhang, J. P., ... Gaska, R. (2005, May). Low frequency noise of light emitting diodes. In Noise in Devices and Circuits III (Vol. 5844, pp. 75-85). International Society for Optics and Photonics.

46 See online supporting information Table 1.

47 de Campos Vidal, B., Mello, M. L. S., Caseiro-Filho, A. C., Godo, C. (1980). Anisotropic properties of the myelin sheath. Acta histochemica, 66(1), 32-39.

48 Maturana, L. G., Pierucci, A., Simões, G. F., Vidigal, M., Duek, E. A., Vidal, B. C., Oliveira, A. L. (2013). Enhanced peripheral nerve regeneration by the combination of a polycaprolactone tubular prosthesis and a scaffold of collagen with supramolecular organization. Brain and behavior, 3(4), 417-430.

49 Blanke, N., Go, V., Rosene, D. L., Bigio, I. J. (2021). Quantitative birefringence microscopy for imaging the structural integrity of CNS myelin following circumscribed cortical injury in the rhesus monkey. Neurophotonics, 8(1), 015010.

50 Jacques, S. L. (2013). Optical properties of biological tissues: a review. Physics in Medicine Biology, 58(11), R37.

51 Ntziachristos, V. (2010). Going deeper than microscopy: the optical imaging frontier in biology. Nature methods, 7(8), 603-614.

52 Mesradi, M., Genoux, A., Cuplov, V., Abi-Haidar, D., Jan, S., Buvat, I., Pain, F. (2013). Experimental and analytical comparative study of optical coefficient of fresh and frozen rat tissues. Journal of biomedical optics, 18(11), 117010.

53 Genina, E. A., Bashkatov, A. N., Tuchina, D. K., Dyachenko, P. A., Navolokin, N., Shirokov, A., ... Tuchin, V. V. (2019). Optical properties of brain tissues at the different stages of glioma development in rats: pilot study. Biomedical optics express, 10(10), 5182-5197.

54 Rich, L. R., Brown, A. M. (2018). Fibre sub-type specific conduction reveals metabolic function in mouse sciatic nerve. The journal of physiology, 596(10), 1795-1812.

55 Haninec, P. (1986). Undulating course of nerve fibres and bands

of Fontana in peripheral nerves of the rat. Anatomy and embryology, 174(3), 407-411.

56 Cohen, L. B., Hille, B., Keynes, R. D. (1969). Light scattering and birefringence changes during activity in the electric organ of Electrophorus electricus. The Journal of physiology, 203(2), 489-509.

57 Von Muralt, A. (1975). The optical spike. Philosophical Transactions of the Royal Society of London. B, Biological Sciences, 270(908), 411-423.

58 Landowne, D. (1985). Molecular motion underlying activation and inactivation of sodium channels in squid giant axons. The Journal of membrane biology, 88(2), 173-185.

59 Cohen, L. B., Hille, B., Keynes, R., Landowne, D., Rojas, E. (1971). Analysis of the potential-dependent changes in optical retardation in the squid giant axon. The Journal of physiology, 218(1), 205-237.

60 Poliak, S., Peles, E. (2003). The local differentiation of myelinated axons at nodes of Ranvier. Nature Reviews Neuroscience, 4(12), 968-980.

61 Stumpp, L., Smets, H., Vespa, S., Cury, J., Nonclercq, A. (2021). Vagus nerve electroneurogram-based detection of acute pentylenetetrazol induced seizures in rats. Brain Stimulation: Basic, Translational, and Clinical Research in Neuromodulation, 14(6), 1725-1726.